

# Scanning Probe Microscopy of Cleaved Molybdates: $\alpha$ - $\text{MoO}_3(010)$ , $\text{Mo}_{18}\text{O}_{52}(100)$ , $\text{Mo}_8\text{O}_{23}(010)$ , and $\eta$ - $\text{Mo}_4\text{O}_{11}(100)$

Richard L. Smith and Gregory S. Rohrer<sup>1</sup>

*Department of Materials Science and Engineering, Carnegie Mellon University, Pittsburgh, Pennsylvania 15213-3890*

Received November 7, 1995; in revised form March 7, 1996; accepted March 12, 1996

Scanning probe microscopy was used to examine the cleaved surfaces of four binary molybdates:  $\alpha$ - $\text{MoO}_3(010)$ ,  $\text{Mo}_{18}\text{O}_{52}(100)$ ,  $\text{Mo}_8\text{O}_{23}(010)$ , and  $\eta$ - $\text{Mo}_4\text{O}_{11}(100)$ . The  $\text{Mo}_{18}\text{O}_{52}(100)$  and  $\text{Mo}_8\text{O}_{23}(010)$  surfaces were imaged in air and vacuum using scanning tunneling microscopy (STM). The contrast associated with two types of surface/crystallographic shear (CS) plane intersections has been unambiguously identified; shear normal to the surface creates a line of vertical relief 1.5 Å high and shear in the surface plane creates a line of dark contrast. The contrast from the surface/CS plane intersection arises, in part, from local variations in the electronic properties. These signatures are easily distinguished from features on the fully oxidized  $\alpha$ - $\text{MoO}_3(010)$  surface. STM images of  $\eta$ - $\text{Mo}_4\text{O}_{11}(100)$  reveal a surface terminated by tetrahedral groups. In each case, we find that the atomic-scale contrast can be interpreted based on the arrangement of surface polyhedra that is expected to result from cleavage of the longest, weakest bonds. © 1996 Academic Press, Inc.

## INTRODUCTION

Molybdenum oxides and mixed metal molybdates are used as catalysts for a number of partial oxidation reactions (1). Studies designed to quantify the relative reactivity of different  $\text{MoO}_3$  facets have led to the conclusion that the surface properties of this compound are surface structure sensitive (2–7). Surface structure determinations, which appear necessary to identify the mechanism of this structure-sensitivity, are complicated by the fact that stoichiometry compensating structural defects are integral components of the active material's surface; when an adsorbed hydrocarbon is oxidized, the catalyst itself is reduced and a defect must be created on the surface. In the near stoichiometric region,  $\text{MoO}_3$  reduction is compensated by oxygen vacancies. Further from stoichiometry, however, transmission electron microscopy has shown that crystallographic shear (CS) planes are the compensating defect (8, 9). Thus, characterization of the relevant surfaces in-

volves determining the population and distribution of these defects.

Scanning probe microscopy (SPM), a term we use here to refer collectively to scanning tunneling microscopy (STM) and atomic force microscopy (AFM), can potentially be used to identify atomic-scale defects on substoichiometric molybdate surfaces. It is, however, necessary to first establish precedents that can be used for image interpretation; this is the objective of the present paper. Herein, we describe the contrast that is observed in STM and AFM images of four stoichiometric molybdenum oxide binary phases:  $\alpha$ - $\text{MoO}_3(010)$ ,  $\text{Mo}_{18}\text{O}_{52}(100)$ ,  $\text{Mo}_8\text{O}_{23}(010)$ , and  $\eta$ - $\text{Mo}_4\text{O}_{11}(100)$ . We take the (010) surface of the most oxidized phase as the "ideal" surface structure, a corner-sharing arrangement of  $\text{MoO}_6$  octahedra similar to a {100} layer of the  $\text{ReO}_3$  structure. The next two phases,  $\text{Mo}_{18}\text{O}_{52}$  and  $\text{Mo}_8\text{O}_{23}$ , contain CS planes that intersect the surface in two distinct ways. In the first structure, there is a component of the shear normal to the surface plane so that in addition to changing the coordination environment of the atoms on the CS plane, the shear creates some surface relief. In the second structure, the shear lies entirely in the surface plane and there is no topographic relief. The final phase,  $\eta$ - $\text{Mo}_4\text{O}_{11}$ , is distinguished from the other three because its surface is terminated entirely by tetrahedral  $\text{MoO}_4$  groups instead of octahedral  $\text{MoO}_6$  groups. The remainder of this section contains a more detailed comparison of the relevant crystal structures and a brief summary of previous studies of the molybdenum oxide surfaces.

### (a) Structural Chemistry of the Molybdenum Oxides

The structural chemistry of the molybdenum oxides was described several decades ago in a series of papers by Khilborg (10–15) and the relevant structural parameters for the phases of interest are summarized in Table 1. These structures can be thought of as relatives of the  $\text{ReO}_3$  ( $D0_6$ ) structure, which is a three dimensional corner-sharing octahedral network. The fully oxidized phase,  $\alpha$ - $\text{MoO}_3$ , has the layered structure illustrated in Fig. 1 (11). Each layer is composed of two corner-sharing octahedral nets that

<sup>1</sup> To whom correspondence should be addressed.

TABLE 1  
Structural and Electronic Properties of Selected Molybdates

Phase	Space group	Lattice parameters <sup>a</sup>	Refined parameters	Specific resistivity
$\alpha$ -MoO <sub>3</sub>	<i>Pbnm</i> (no. 62)	$a = 3.963 \text{ \AA}$ $b = 13.85 \text{ \AA}$ $c = 3.696 \text{ \AA}$	$a = 3.966(1) \text{ \AA}$ $b = 13.87(1) \text{ \AA}$ $c = 3.701(1) \text{ \AA}$	Insulating
Mo <sub>18</sub> O <sub>52</sub> <sup>b</sup> (vapor grown)	<i>P</i> $\bar{1}$ (no. 2)	$a = 8.145 \text{ \AA}$ $b = 11.89 \text{ \AA}$ $c = 21.23 \text{ \AA}$ $\alpha = 102.67^\circ$ $\beta = 67.82^\circ$ $\gamma = 109.97^\circ$	$a = 8.097(24) \text{ \AA}$ $b = 11.812(28) \text{ \AA}$ $c = 21.415(43) \text{ \AA}$ $\alpha = 102.22(22)^\circ$ $\beta = 68.43(21)^\circ$ $\gamma = 109.46(28)^\circ$	78.1 $\Omega$ -cm
Mo <sub>8</sub> O <sub>23</sub>	<i>P2/a</i> (no. 13)	$a = 16.88 \text{ \AA}$ $b = 4.052 \text{ \AA}$ $c = 13.39 \text{ \AA}$ $\beta = 106.19^\circ$	$a = 16.91(1) \text{ \AA}$ $b = 4.055(2) \text{ \AA}$ $c = 13.40(1) \text{ \AA}$ $\beta = 106.36(4)^\circ$	7.01 $\Omega$ -cm
$\eta$ -Mo <sub>4</sub> O <sub>11</sub>	<i>P2<sub>1</sub>/a</i> (no. 14)	$a = 24.54 \text{ \AA}$ $b = 5.439 \text{ \AA}$ $c = 6.701 \text{ \AA}$ $\beta = 94.28^\circ$	$a = 24.54(1) \text{ \AA}$ $b = 5.442(3) \text{ \AA}$ $c = 6.707(3) \text{ \AA}$ $\beta = 94.37(5)^\circ$	$1.66 \times 10^{-4} \text{ \Omega-cm}$

<sup>a</sup> From Ref. (10).

<sup>b</sup> Lattice parameters for Li-doped crystals were comparable and the resistivity was 17.2  $\Omega$ -cm.

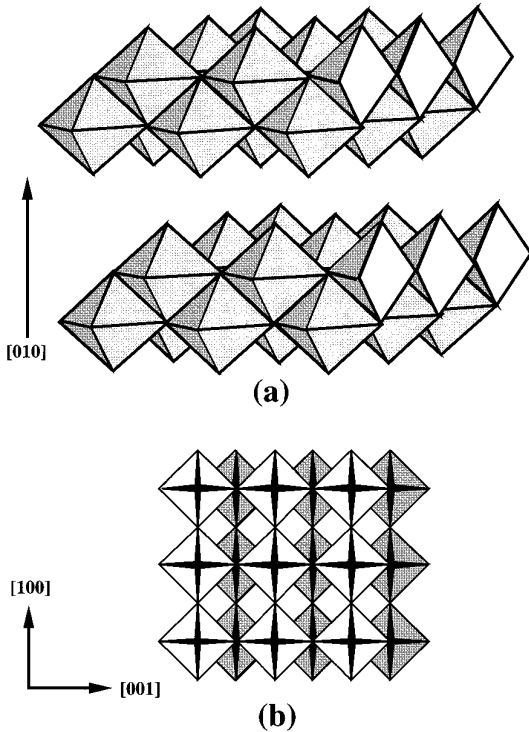


FIG. 1. A polyhedral representation of the  $\alpha$ -MoO<sub>3</sub> structure. (a) The structure is built of double octahedral layers stacked along [010]. The spacing between adjacent double layers is 6.9  $\text{\AA}$ . (b) A projection on the (010) plane shows two superimposed rectangular nets of corner-sharing octahedra. The shaded net is below the unshaded one.

link by sharing edges along [001]. The adjacent layers along [010] are linked only by weak van der Waals forces. In projection along [010] (see Fig. 1b), one sees a corner-sharing net that is characteristic of the ReO<sub>3</sub> structure. The feature that distinguishes the  $\alpha$ -MoO<sub>3</sub> structure from the ReO<sub>3</sub> structure is the linkages along [010]; each square octahedral net in the ReO<sub>3</sub> structure is linked along [010] by corner-sharing at the apical positions.

The Mo<sub>18</sub>O<sub>52</sub> (12) structure and the Mo<sub>8</sub>O<sub>23</sub> (13) structure can be derived from the fully oxidized structures by CS operations, as illustrated in Fig. 2. Within the context of the higher molybdenum oxides, we can think of CS as transforming a subset of octahedra, along specific planes, from a corner-sharing to an edge-sharing arrangement. This transformation reduces the average O coordination number and, therefore, involves reduction. The shear operation in each crystal is characterized by a translation vector (the magnitude and direction of the shear) and a plane of propagation. For example, the Mo<sub>18</sub>O<sub>52</sub> structure derives directly from the  $\alpha$ -MoO<sub>3</sub> by introducing shear of  $\frac{1}{2} \langle 1\bar{1}0 \rangle \{3\bar{5}1\}$ . The new cell is indexed so that  $[010]_{\text{MoO}_3} \parallel [100]_{\text{Mo}_{18}\text{O}_{52}}$ . The Mo<sub>8</sub>O<sub>23</sub> structure is derived by a CS operation of  $\frac{1}{2} \langle 010 \rangle \{102\}$  and the new cell is indexed so that  $[010]_{\text{MoO}_3} \parallel [010]_{\text{Mo}_8\text{O}_{23}}$ .

There are noteworthy differences between these two shear structures. While the Mo<sub>18</sub>O<sub>52</sub> structure is derived from the  $\alpha$ -MoO<sub>3</sub> structure, the Mo<sub>8</sub>O<sub>23</sub> structure is derived from the ReO<sub>3</sub> structure. This is an important distinction because the layers that make up the structure Mo<sub>8</sub>O<sub>23</sub> (see

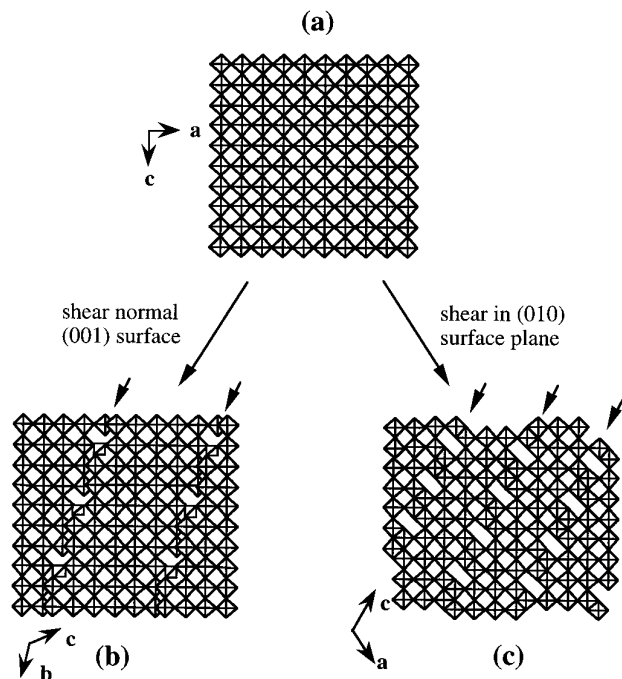


FIG. 2. The relationship between a layer of the  $\text{MoO}_3$  structure, viewed along  $[010]$  (a), a layer of the  $\text{Mo}_{18}\text{O}_{52}$  structure, viewed along  $[100]$  (b), and a layer of the  $\text{Mo}_8\text{O}_{23}$  structure, viewed along  $[010]$  (c).  $CS$  operations (see text for details) are used to derive the reduced structures. Arrows have been used to guide the eye to the  $CS$  planes.

Fig. 2c) are joined along  $[010]$  by corner-shared connections at the apical O position. Thus,  $\text{Mo}_8\text{O}_{23}$  is a three-dimensionally bonded structure that does not contain a van der Waals gap as the  $\text{Mo}_{18}\text{O}_{52}$  and  $\alpha\text{-MoO}_3$  structures do. Another difference that is important for the interpretation of the SPM observations described here is the direction of the shear vector with respect to the cleavage plane. The shear in  $\text{Mo}_{18}\text{O}_{52}$  has a component normal to the  $(100)$  surface plane that produces a shear step (its height equal to the radius of an O ion) along the line of intersection. The direction of the shear in  $\text{Mo}_8\text{O}_{23}$ , on the other hand, lies in the  $(010)$  surface plane and, therefore, does not produce a shear step on the surface. In the  $\text{Mo}_{18}\text{O}_{52}$  structure, the lines formed where the shear planes intersect the surface are oriented along the  $[010]$  direction and are spaced at  $21 \text{ \AA}$  intervals along the  $[001]$  direction. In the  $\text{Mo}_8\text{O}_{23}$  structure, these lines of intersection are oriented along  $[001]$  and are spaced at  $13 \text{ \AA}$  intervals along the  $[100]$  direction. Although both types of  $CS$  planes would be classified as defects if distributed inhomogeneously in reduced  $\text{MoO}_{3-x}$ , they are periodic structural components of the shear phases and can, therefore, be unambiguously identified. The identification of surface/ $CS$  plane intersections in these ordered structures will simplify the inter-

pretation of SPM images of inhomogeneously reduced surfaces.

The  $\eta\text{-Mo}_4\text{O}_{11}$  structure provides an example of another mechanism that is used to increase the metal-to-oxygen ratio. Rather than having infinite slabs of the  $\text{ReO}_3$  structure linked together as  $CS$  planes, as is the case for the shear phases, the slabs are linked together by planes of  $\text{MoO}_4$  tetrahedra (14). In the  $\eta\text{-Mo}_4\text{O}_{11}$  structure, these planes are spaced at  $12 \text{ \AA}$  intervals and inspection of Fig. 3a allows one to see that although it is a three-dimensionally bonded structure, the lowest density of bonds is in the tetrahedral layers parallel to  $(100)$ . We assume, therefore, that when crystals are cleaved to expose  $(100)$  surfaces, they will be terminated by tetrahedral  $\text{MoO}_4$  groups. A view parallel to the  $(100)$  plane (see Fig. 3b) shows that the tetrahedral  $\text{MoO}_4$  groups are elevated farthest from the surface plane and the view projected on  $(100)$ , shown in Fig. 3c, shows that these groups form a rectangular net.

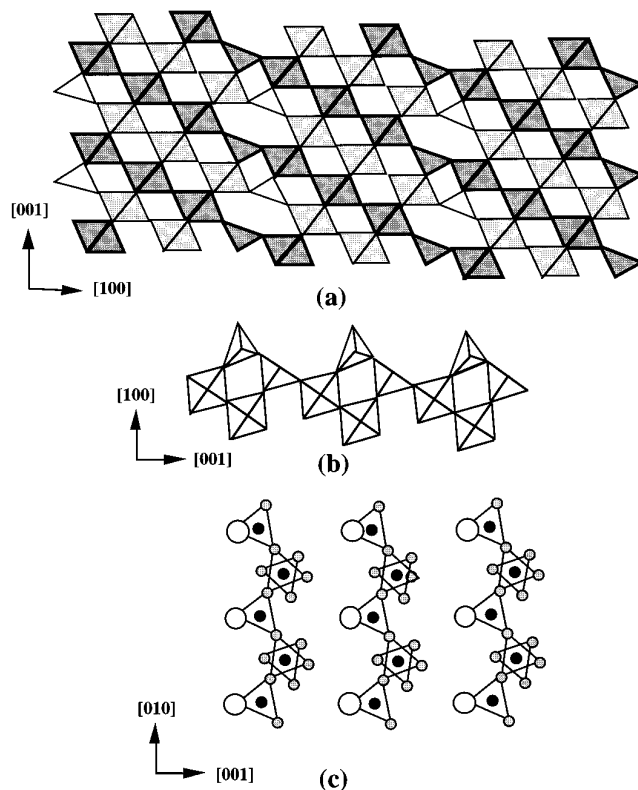


FIG. 3. The  $\eta\text{-Mo}_4\text{O}_{11}$  Structure. (a) An  $[010]$  projection showing the planes of tetrahedral groups that separate  $\text{ReO}_3$ -like blocks of the structure. The polyhedra with different shades are at different vertical levels. (b) A view parallel to the  $(100)$  surface that is expected to form during cleavage. (c) A plan-view of the  $(100)$  surface. Circles represent O at the vertices of surface polyhedra. The O atoms represented by the largest circles, at the vertices of the tetrahedra, are elevated further from the surface than the others. Mo atom positions are represented by the small black circles.

### (b) Previous Studies of Molybdate Surfaces

The interesting surface properties of  $\text{MoO}_3$  have, of course, motivated earlier structural studies by more conventional surface analysis methods (16–21). Specifically, the results of low energy electron diffraction (LEED) (16, 17), electron energy loss spectroscopy, X-ray photoelectron spectroscopy, ultraviolet photoelectron spectroscopy (UPS) (16), angle resolved UPS (18), and reflection high energy electron diffraction (RHEED) (17) experiments have been reported for  $\text{MoO}_3$ . RHEED data have also been reported for  $\text{Mo}_{18}\text{O}_{52}$  (19). The electron diffraction results indicate that the ideal  $\text{MoO}_3(010)$  surface has a  $1 \times 1$  structure. However, the stoichiometric surface is difficult to prepare and not entirely stable during analysis. Separate research groups have noted that in vacuum, the surface is easily damaged by the electron probes (16, 17). For this reason, most of the reported results are actually characteristic of nonstoichiometric surfaces.

A number of SPM observations of molybdate surfaces have also been reported. Atomic-scale resolution AFM images of a single layer of  $\text{MoO}_3(010)$ , formed by oxidation of the  $\text{MoS}_2(0001)$  surface, demonstrated the expected ( $1 \times 1$ ) rectangular surface repeat unit (22). In this case, there was a one-to-one correspondence between the bright spots on the image and the positions of the  $\text{MoO}_6$  octahedral groups that make up this surface plane. There have also been ambient STM studies of some ternary alkali molybdate bronzes,  $A_{0.3}\text{MoO}_3$  (23–26) and  $A_{0.9}\text{Mo}_6\text{O}_{17}$  (25), where  $A$  is an alkali metal. While the focus of these studies has been on nanolithography (24, 25) and charge density wave phenomena (26), atomic-scale resolution images were also reported. In all of these reports, images were formed using conduction band states near the Fermi level and the authors noted a one-to-one correspondence between the configuration of bright spots in the images and the expected positions of polyhedra on the cleaved surfaces. Thus, it was assumed that the positions of bright contrast in the image marked the positions of the surface octahedra and tetrahedra, in axial alignment, terminated by an apical O. A similar interpretation has been applied to other transition metal oxides and justified by simple calculations (27, 28). Even though the O  $2p$  orbitals make a minority contribution to the conduction band states, they are advantageously positioned at the apices of the surface polyhedra and, being closer to the tip, they dominate the contrast. Following this interpretation, we assume that both the metal and the O contribute to the tunnel current and it is the  $\text{MoO}_x$  polyhedra as a whole that are imaged.

The current authors previously reported ultra-high-vacuum (UHV) STM images of the  $\text{Mo}_{18}\text{O}_{52}(100)$  surface (29). As with the ternary molybdate surfaces studied in air, we

found a one-to-one correlation between the bright spots in the image contrast and the polyhedral groups expected to be found on the surface. We have since expanded on our previous findings and in this paper we compare these additional observations of the  $\text{Mo}_{18}\text{O}_{52}(100)$  surface with results from three other binary molybdate surfaces:  $\alpha\text{-MoO}_3(010)$ ,  $\text{Mo}_8\text{O}_{23}(010)$ , and  $\eta\text{-Mo}_4\text{O}_{11}(100)$ . In addition to being able to identify different types of surface/ $CS$  plane intersections, we find that the atomic-scale contrast can be interpreted based on the arrangement of surface polyhedra that is expected to result from cleavage of the longest, weakest bonds. We also present a comparison of images recorded in UHV and air, and describe the results of a spatially resolved tunneling spectroscopy experiment used to probe the local electronic properties of the surface/ $CS$  plane intersection.

## EXPERIMENTAL PROCEDURE

### (a) Crystal Growth and Characterization

All of the images presented in this paper are from cleaved facets of single crystals grown in our lab. The nominally pure phases, which include  $\alpha\text{-MoO}_3$ ,  $\text{Mo}_{18}\text{O}_{52}$ ,  $\text{Mo}_8\text{O}_{23}$ , and  $\eta\text{-Mo}_4\text{O}_{11}$ , were grown from the vapor in sealed quartz tubes using similar procedures that were developed on the basis of previously published reports (30, 31). In each case, well-ground  $\text{MoO}_3$  and Mo metal were combined in the appropriate ratio, dehydrated in vacuum, and then sealed in an evacuated quartz ampoule with a small amount of an iodine or chlorine source to act as a mineralizer. The iodine source was solid  $\text{I}_2$  crystals and the chlorine source was solid  $\text{TeCl}_4$ , which decomposes at the reaction temperature. The quartz ampoules had an approximately 10 cm length and a 13 mm inner diameter. Crystal growth occurred while annealing the ampoules for times that varied from several days to a week. The relevant details for each of the steps in the procedure are summarized in Table 2. It is noteworthy that in most experiments, more than one of the molybdate phases grew in each tube. However, because each phase has a distinct habit and color, crystals of different composition are easily separated.

Li-doped  $\text{Mo}_{18}\text{O}_{52}$  crystals, with a higher conductivity than the pure phase, were grown by slowly cooling a molten mixture of molybdenum trioxide and Li intercalated molybdenum oxide.  $\text{MoO}_3$  and  $\text{Li}_{0.25}\text{MoO}_3$  (prepared by Na intercalation and ion exchange in aqueous LiCl) were combined in a 6.25 to 1 molar ratio, mixed, dried under vacuum, and sealed in an evacuated quartz tube with an 11 mm inner diameter and an 80 mm length. The mixture was then heated to  $850^\circ\text{C}$  for 4 hr and cooled to  $400^\circ\text{C}$  at approximately  $4.5^\circ\text{C/hr}$ . The solid product contained mm-sized black crystals, which X-rays revealed to be  $\text{Mo}_{18}\text{O}_{52}$ , in a finer grained matrix of  $\text{MoO}_3$ . We differentiate these melt-grown  $\text{Mo}_{18}\text{O}_{52}$  crystals from the vapor-grown crys-

TABLE 2  
Crystal Growth Parameters

Phase	Charge stoichiometry	Charge size, g/cm <sup>3</sup>	Mineralizer	Hot zone temp., °C	Temp. gradient, °C	Morphology
$\alpha$ -MoO <sub>3</sub>	MoO <sub>3</sub>	0.09	TeCl <sub>4</sub>	520	20	Clear plates
Mo <sub>18</sub> O <sub>52</sub>	MoO <sub>2.882±.008</sub>	0.06	I <sub>2</sub>	700 ± 30	10	Black plates
Mo <sub>8</sub> O <sub>23</sub>	MoO <sub>2.88±0.01</sub>	0.05	I <sub>2</sub>	690	0	Barrel shaped
$\eta$ -Mo <sub>4</sub> O <sub>11</sub>	MoO <sub>2.76</sub>	0.02	TeCl <sub>4</sub>	525	35	Purple plates

tals because their electronic conductivity is four times greater. The most likely reason for this is that they are intercalated with a small amount of Li (present in the melt) which donates electrons to the conduction band.

Representative crystals of each phase were pulverized for powder diffraction analysis. Each crystal was phase pure (all peaks could be indexed to a single cell) and unambiguously identified by its characteristic diffraction pattern. The measured lattice parameters, refined from at least 17 peaks in each pattern, are given in Table 1 and compare favorably to those originally established by Khilborg (10–15). The room temperature specific electronic resistivity of each phase was measured using the four point probe technique and these results are also included in Table 1. These results are consistent with available data and reflect the general trend that as the metal-to-oxygen ratio increases, the conductivity increases (15, 32, 33).

#### (b) SPM Analysis

All of the SPM images presented in this paper were recorded on surfaces prepared by cleavage. Because they are layered compounds,  $\alpha$ -MoO<sub>3</sub> and Mo<sub>18</sub>O<sub>52</sub> are easily cleaved with adhesive tape. The three-dimensionally bonded compounds, Mo<sub>8</sub>O<sub>23</sub> and  $\eta$ -Mo<sub>4</sub>O<sub>11</sub>, are mechanically more robust and must be cleaved with a razor blade. Because pure, stoichiometric MoO<sub>3</sub> is electronically insulating, images can be formed only using AFM. The AFM was operated in contact mode using pyramidal Si<sub>3</sub>N<sub>4</sub> probes. The other three phases are electronic conductors and can be imaged with ambient or UHV STM. All STM images presented here were recorded in the constant current mode, using currents of approximately 1 nA. Atomic-scale resolution images of all three of the reduced compounds were reproducibly recorded in the ambient. Mo<sub>18</sub>O<sub>52</sub> and Mo<sub>8</sub>O<sub>23</sub> were also imaged at high resolution in UHV. The Mo<sub>18</sub>O<sub>52</sub> crystals were cleaved immediately before insertion into the vacuum chamber via a load lock. The Mo<sub>8</sub>O<sub>23</sub> crystals were cleaved in a N<sub>2</sub> filled glove bag immediately before insertion into the vacuum chamber. All STM images were produced using clipped Pt–Ir tips and those presented are representative of many observa-

tions on multiple crystals. High frequency noise (smaller than interatomic spacings) and a background plane have been subtracted from each image.

Spatially resolved tunneling spectra were recorded while imaging the Mo<sub>18</sub>O<sub>52</sub> surface. During this experiment, the scans used to collect topographic data for the image are momentarily interrupted at preselected positions, the feedback loop is switched off, and the current is measured as a function of the junction bias. After the current–voltage (*IV*) curve is measured, the feedback loop is re-engaged and the imaging process continues. By recording the *IV* curves in this way, they can be correlated with specific topographic features on the image.

## RESULTS

#### (a) MoO<sub>3</sub>(010)

Cleaved MoO<sub>3</sub>(010) surfaces are characterized by atomically flat terraces over areas as large as 200  $\mu\text{m}^2$ . MoO<sub>3</sub> is a micaceous material; instead of the relatively strong primary Mo–O bonds breaking, cleavage occurs at the weak van der Waals bonds between the adjacent double octahedral layers. In this process, two identical O-terminated surfaces are formed. Some steps are invariably created during cleavage and the majority of them are oriented along [001], the direction along which the octahedra share edges with the plane below. Steps with this orientation can be formed by breaking bonds between Mo and doubly coordinate O at the shared corners of the octahedra. The formation of perpendicular steps (along [100]) would require twice as many Mo–O bonds to be broken. Such steps presumably have a higher energy and, therefore, form less frequently. The contact mode AFM image in Fig. 4a shows an area where atomically flat terraces are separated by a step. The van der Waals gap between adjacent MoO<sub>3</sub> layers along the [010] direction occurs every 6.9 Å and this is the smallest step observed on the cleaved surfaces.

Because only weak van der Waals bonds are broken to form this surface, it has a very low energy and significant atomic relaxation is not expected. Based on knowledge of the bulk structure, we expect the surface plane to be

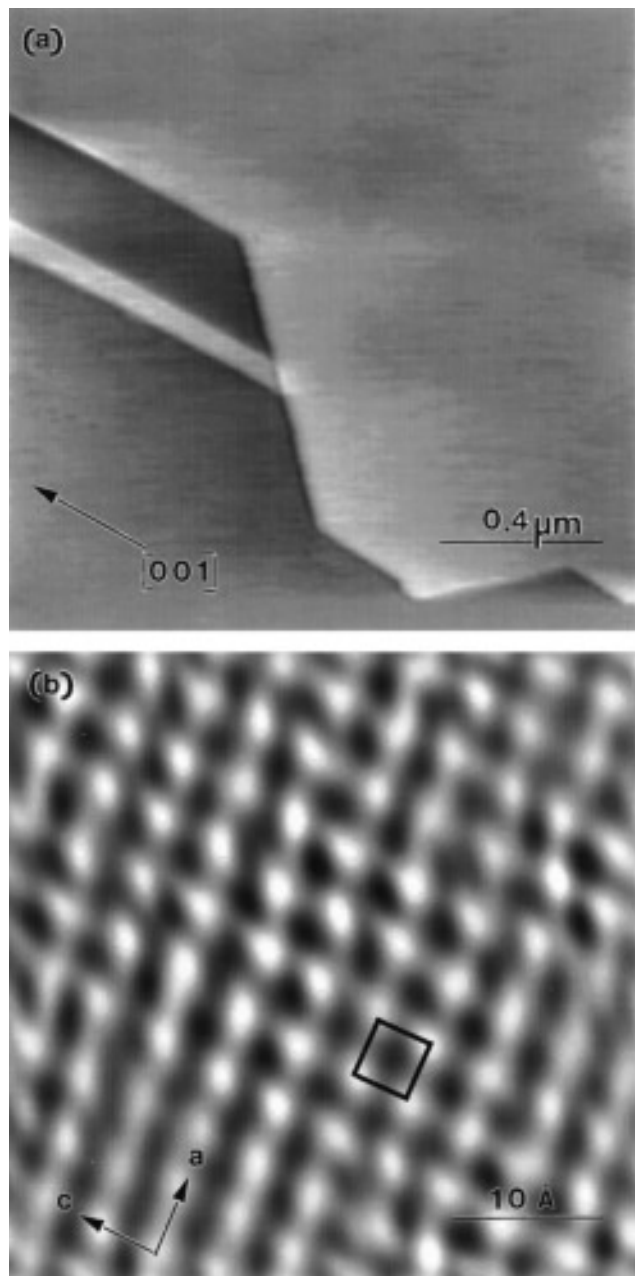


FIG. 4. Two contact AFM images of the cleaved  $\alpha$ - $\text{MoO}_3(010)$  surface. Similar images were recorded with force setpoints in the range of 10 to 40 nN. (a) A  $1.6 \mu\text{m} \times 1.6 \mu\text{m}$  image of the cleaved surface showing two terraces separated by a step, approximately  $7 \text{ \AA}$  high. (b) A  $42 \text{ \AA} \times 42 \text{ \AA}$  image shows a pattern of atomic-scale contrast with an approximately square repeat unit. Because this image was formed from the difference signal, the vertical scale is arbitrary.

terminated by a layer of O atoms at the apices of octahedral groups. The O atoms are more than  $1.6 \text{ \AA}$  above the next layer of atoms and should be arranged to form a rectangular (nearly square) repeat unit,  $3.96 \text{ \AA} \times 3.70 \text{ \AA}$ . Atomic-scale resolution contrast can routinely be observed in AFM

images of the flat terraces. The image shown in Fig. 4b was formed using the difference signal between the deflection set point and the actual deflection. Simultaneously recorded topographic images (formed from the output of the feedback loop) showed the same contrast features; a nearly square repeat unit with dimensions of approximately  $4 \text{ \AA} \times 4 \text{ \AA}$ . This observation of a  $1 \times 1$  repeat unit is identical to the reported LEED results (16, 17) and the earlier AFM results on oxidized  $\text{MoS}_2$  (22). We should mention that the mechanism by which atomic-scale contrast is formed in ambient AFM images remains a subject of debate. Many believe that the contrast is formed by a cooperative interaction of the tip with a large area of the surface (34, 35). Even so, there are numerous examples in which the features in atomic-scale resolution AFM images can be correlated to bulk structure (36). In the case of  $\text{MoO}_3(010)$ , there is a one-to-one correlation between the white contrast features on the image and the expected positions of surface octahedra.

In addition to well developed basal facets, the  $\text{MoO}_3$  crystals used in this study had optically smooth lateral facets that could be indexed approximately as  $(570)$  planes. However, contact AFM images of the as-grown facets revealed that these macroscopically “flat” surfaces were actually made up of parallel steps oriented in the  $[001]$  direction. Although the spacing and height of the steps is irregular, their orientation is fixed, as illustrated in the example shown in Fig. 5. The presence of these steps is interesting in light of the proposed mechanisms for the partial oxidation of hydrocarbons on  $\text{MoO}_3$  surfaces. For example, it has been proposed that hydrocarbon activation takes place on side  $(100)$  and  $(101)$  facets while oxygen

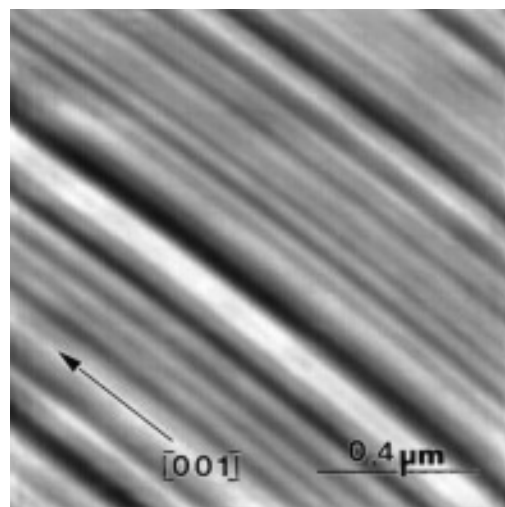


FIG. 5. A  $1.25 \mu\text{m} \times 1.25 \mu\text{m}$  AFM image of a lateral growth facet of  $\alpha$ - $\text{MoO}_3$ , indexed approximately to  $(570)$ . The vertical scale from black-to-white is to  $140 \text{ \AA}$ . The lines of contrast correspond to steps oriented along the  $[001]$  axis of the crystal.

insertion takes place on the (010) basal plane (4). The microfaceted planes observed here would place both types of sites in close proximity.

(b)  $Mo_{18}O_{52}(100)$

Cleaved  $Mo_{18}O_{52}(100)$  surfaces are also flat over many micrometers. When steps are encountered, they are invariably oriented along the [010] axis of the crystal. This is the direction along which the CS planes intersect the surface plane. The crystal structure of this compound is closely related to that of  $MoO_3$ ; it also has double octahedral layers that are linked only by weak van der Waals bonds. Thus, the cleaved (100) surfaces should be fully terminated by oxygen and show an  $MoO_3$ -like structure between surface/CS plane intersections. The contrast in both STM and AFM images of this surface is dominated by 1.5 Å vertical steps, oriented along the [010] axis, spaced at approximately 20 Å intervals. Because of their spacing and orientation, we assign this contrast to the positions where CS planes intersect the surface.

High resolution UHV STM images (for example, see Fig. 6a) show additional contrast within the terraces. Rows of white contrast have a 3.8 Å period, just as do the rows of  $MoO_6$  octahedra in the structure. At the end of every third row a brighter spot occurs with an 11.8 Å periodicity along [010]. This is equivalent to the spacing between the  $MoO_4$  tetrahedral groups that define the vertices of the surface repeat unit. Within experimental error, the surface repeat unit has the same dimensions as the (100) plane of the bulk structure.

Images can also be routinely recorded in air (see Fig. 6b). The contrast in the image of this Li-doped crystal shows the same terrace-shear step structure as Fig. 6a. However, individual round, white contrast features are resolved within each terrace. There is a one-to-one correlation between these features and the corner-sharing octahedra that make up the surface. It is also noteworthy that the contrast associated with the tetrahedral groups in the UHV images is not present. This is a characteristic of all images recorded in air. It is also interesting that when comparing images recorded in air, the images of the Li-doped crystals typically had a higher resolution than images of the undoped crystals. This suggests that the conductivity of nominally pure  $Mo_{18}O_{52}$  is near the lower acceptable limit for high resolution imaging. Finally, we note that while both air and UHV images were recorded by tunneling from occupied states, the highest resolution images in air were formed by tunneling between  $-0.65$  and  $-0.35$  V while the highest resolution images in vacuum were recorded at about  $-1.65$  V.

The image in Fig. 7a was formed in air while simultaneously recording a series of  $IV$  curves. When the tip reached each of 28 evenly spaced positions along the diagonal line

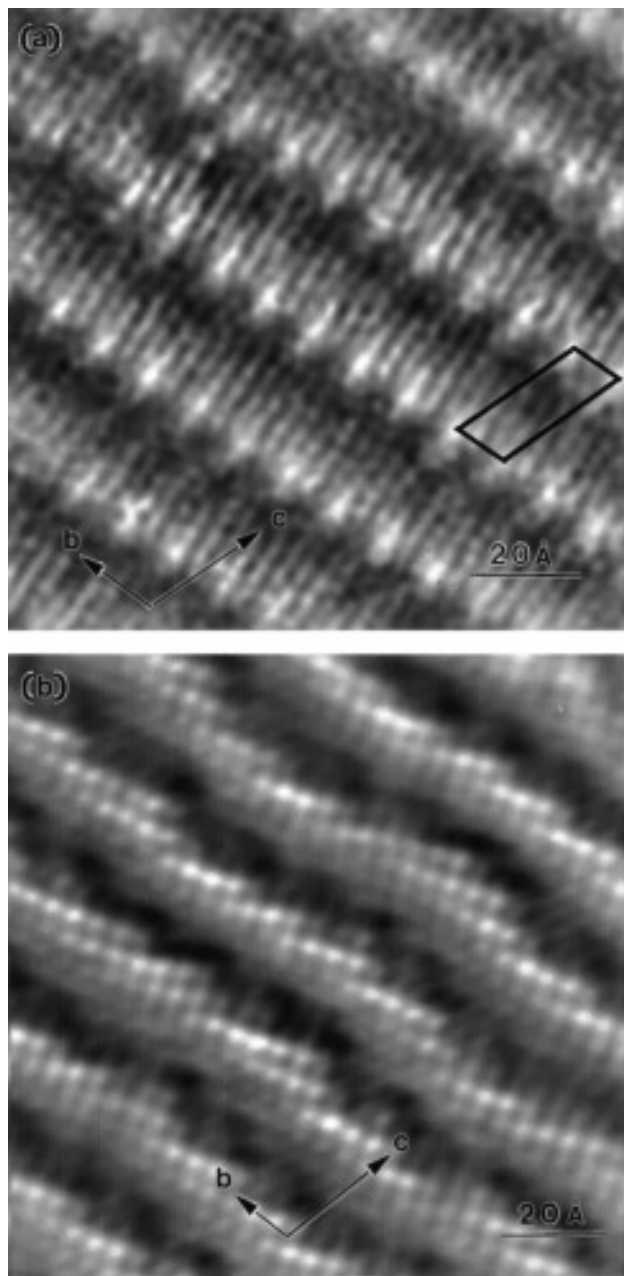


FIG. 6. STM images of the  $Mo_{18}O_{52}(100)$  surface. (a) A  $120 \text{ \AA} \times 120 \text{ \AA}$  image recorded in UHV using a bias of  $-1.65$  V. The vertical distance from black-to-white is 2.5 Å. (b) A  $125 \text{ \AA} \times 125 \text{ \AA}$  image of a Li-doped crystal, recorded in air at a bias of  $-0.41$  V. The vertical height from black-to-white is 3 Å.

marked on the image, it recorded, at constant height, the current while the sample bias was ramped from  $-1.0$  to  $1.0$  V. None of the images that we measured while simultaneously recording spectra had resolution comparable to those in Fig. 6. However, the surface/CS plane intersections were clearly distinguished by the transitions from light to dark contrast. The  $IV$  curves from different loca-

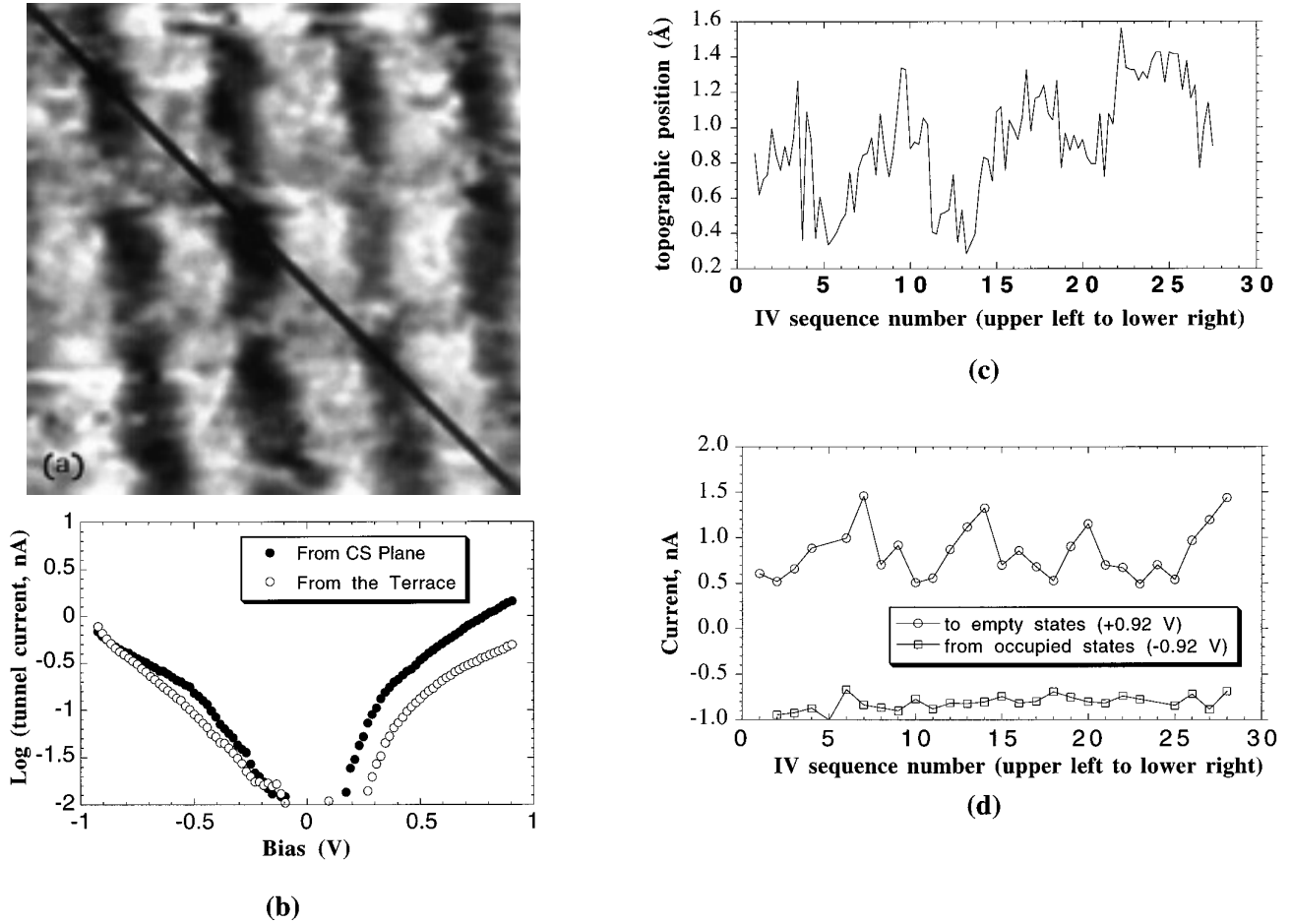
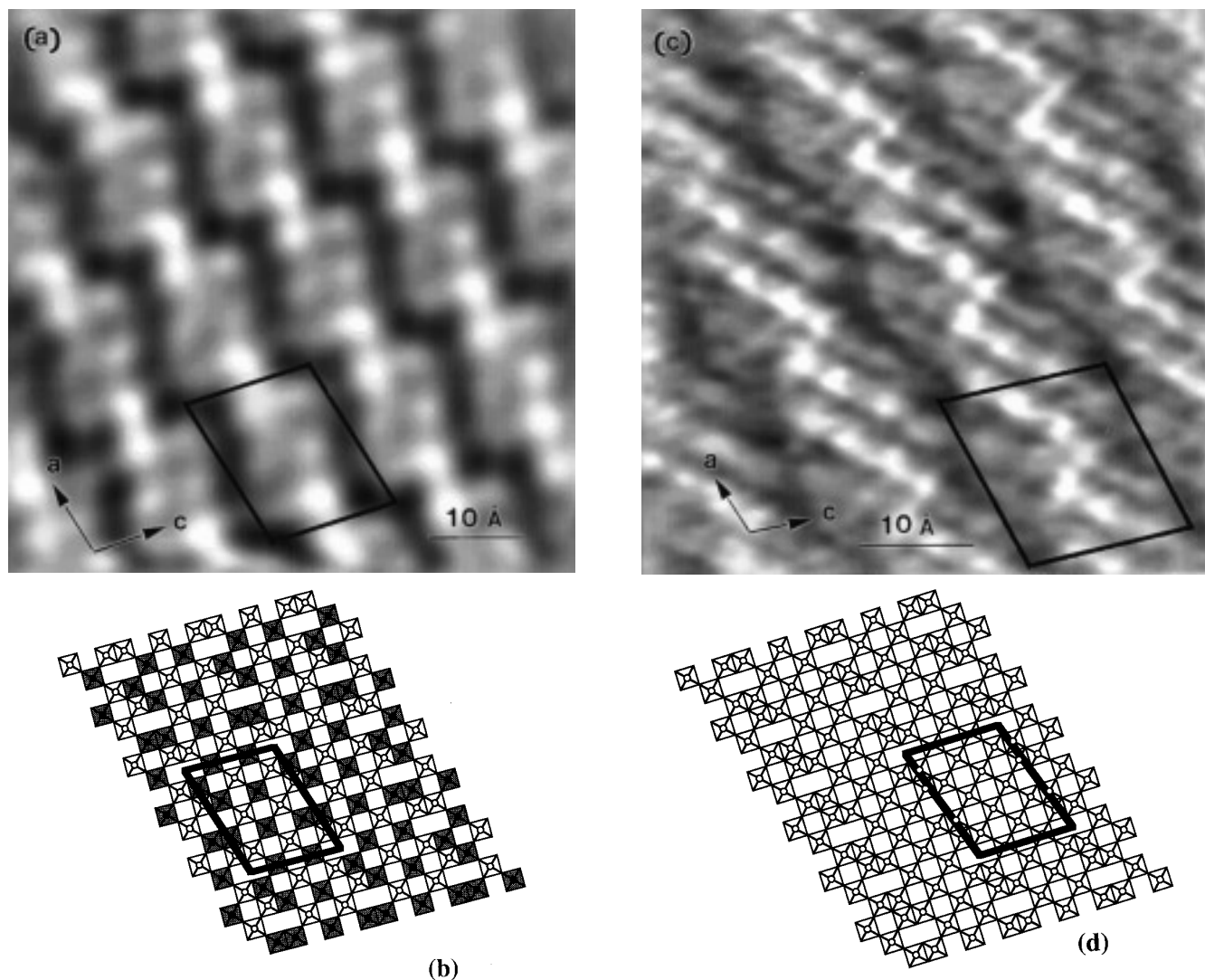


FIG. 7. (a) A  $93 \text{ \AA} \times 93 \text{ \AA}$  STM image of the  $\text{Mo}_{18}\text{O}_{52}(100)$  surface, recorded in air, at a bias of  $-0.68 \text{ V}$ . At 28 evenly spaced points along the indicated diagonal line, an IV curve was measured. (b) Comparison between an IV curve from an area of dark contrast (solid symbols) and an area of light contrast (open symbols). (c) The topography along the line in a. (d) Each point on these curves is taken from one of the IV curves so that the lines give a plot of the current measured at specific biases ( $-0.92$  and  $0.92 \text{ V}$ ) v. distance along the line.

tions on the surface show characteristic differences that are illustrated by the two examples in Fig. 7b; those recorded on the surface/*CS* plane intersection always have increased current when probing unfilled states. To demonstrate that this characteristic was reproduced in all of the spectra, the current level measured at  $0.92 \text{ V}$  was extracted from each of the 28 IV curves and plotted as a function of position in Fig. 7d. This is compared to the current measured at  $-0.92 \text{ V}$ , plotted in the same figure. The current into the unfilled states is clearly correlated to the topography (see Fig. 7c) while the current from the filled states is constant with topography. (The consistency of the filled state measurements is expected since the image was recorded in constant current mode and the set point was  $-0.68 \text{ V}$ .) The current to the empty states peaks at the topographic minima, the locations of the surface/*CS* plane intersections. Thus, the conductance to the empty states locally increases at the positions where the *CS* planes intersect the surface.

### (c) $\text{Mo}_8\text{O}_{23}(010)$

Cleaved  $\text{Mo}_8\text{O}_{23}(010)$  surfaces were also characterized by micrometer-scale large flat areas. However, the morphology of the cleavage surface depended on the direction of the cleave. Most cleaves produced irregularly curved steps that were rarely found on  $\text{MoO}_3$  or  $\text{Mo}_{18}\text{O}_{52}$ . Cleavage along  $[001]$ , however, produces many straight steps oriented along  $[100]$ . Although high-resolution STM images could be recorded in air or UHV, the surface was etched during AFM experiments and all images showed the effect of this degradation. The etching phenomenon appears to be similar to what Parkinson (37) observed in SPM studies of layered chalcogenides. In STM images of these surfaces, two types of contrast can be observed in different places on the same crystal. Examples are shown in Figs. 8a and 8c. We have observed both types of contrast while making images in air by tunneling from filled states at  $-0.7 \text{ V}$ . In vacuum, tunneling at  $1.3 \text{ V}$  into empty states,



**FIG. 8.** STM images of the  $\text{Mo}_8\text{O}_{23}(010)$  surface. (a) An  $58 \text{ \AA} \times 58 \text{ \AA}$  image recorded in UHV using a bias of 1.3 V. The vertical height from black-to-white is 1  $\text{\AA}$  (b) A projected model of the surface, at approximately the same scale as (a), with polyhedra shaded on the basis of the axial displacement of the apical O that connects the layers (c) A  $50 \text{ \AA} \times 50 \text{ \AA}$  image recorded in air at a bias of  $-0.7 \text{ V}$ . The vertical height from black-to-white is 1.5  $\text{\AA}$ . (d) A projected model of the surface, with polyhedra equivalent. The scale is approximately the same as in (d).

only the type of contrast exhibited by Fig. 8a was observed. In both cases, the dimensions of the repeat unit are equivalent, within experimental error, to the dimensions of the (010) projection of the  $\text{Mo}_8\text{O}_{23}$  unit cell. However, the atomic-scale features in the images are clearly different.

By considering the details of the bulk crystal structure, it is possible to identify the most likely surface termination produced when the crystal is cleaved to expose (010) planes. Although  $\text{Mo}_8\text{O}_{23}$  is nominally a three-dimensionally bonded structure, there is significant anisotropy in the axial Mo–O–Mo bonds that link the layers of octahedra along the [010] axis of the crystal. There are 16 such axial linkages per unit cell and in each there are one very strong and short (1.69  $\text{\AA}$ ) Mo–O bond and one longer, weaker

(2.35  $\text{\AA}$ ) contact. For comparison, the shorter of these two Mo–O bonds is similar in length to the bonds between Mo and the singly coordinate apical O atoms (1.67  $\text{\AA}$ ) that terminate the basal plane layers in  $\text{MoO}_3$ . Assuming that the network of longer, weaker bonds is broken, cleavage produces two identical surfaces on which half of the surface polyhedra are  $\text{MoO}_6$  octahedra capped by apical O atoms and the other half are inverted  $\text{MoO}_5$  square pyramids that are not capped by apical O. This ideal termination pattern is illustrated in Fig. 8b where the polyhedra capped by O are white and those without the apical O are shaded.

Considering this termination model, the contrast in the image shown in Fig. 8a can then be understood by making a one-to-one correlation between half of the surface poly-

hedra in the model and the white contrast features on the STM image. In Fig. 8b, we see that both sets of surface polyhedra (for example, consider the white ones) form rows of six octahedra aligned along the  $[201]$  direction. Each repeat unit (the oblique surface unit cell is indicated by the dark lines) contains three of the polyhedra from each of two adjacent rows. One of the rows continues to the cell below and the other to the cell above. An identical pattern of features can be identified in the STM image. Using this correlation, the surface/ $CS$  plane intersections are the dark lines of contrast in the image. It is important to note that the assignment of the dark lines as the surface/ $CS$  plane intersections is not dependent on which subset of the polyhedra are imaged as white spots since the two subsets form the same pattern; it is important only that the two types of polyhedra be imaged differently.

Because the ideal surface is composed of a mixture of capped and uncapped polyhedra, it is comparable to the basal plane of the  $V_2O_5$  structure, which is composed of pairs of inverted and upright square pyramids. STM images of this surface, described in an earlier report, also reveal only half of the surface polyhedra. Based on image simulations, we concluded that it is the upright square pyramids that are imaged as white contrast (28). We expect that the imaging mechanism in this case is similar.

The second type of contrast (see Fig. 8c) can be interpreted by assuming that all of the surface polyhedra are imaged, without distinguishing between those that are terminated by O and those that are not. Within each repeat unit there are rows of white contrast oriented along the  $[10\bar{1}]$  direction. These contrast features have an orientation and spacing identical to the rows of corner-sharing octahedra that make up the structure. For comparison, Fig. 8d shows a model where all of the polyhedra are identical. Using these features as a guide, we again conclude that the surface/ $CS$  plane intersections can be assigned to the dark lines of contrast oriented along the  $[100]$  axis of the crystal. Because this type of contrast can be observed under the same conditions as the other, we assume that there is a difference in the surface structure. Based on the uniformity with which the polyhedra are imaged, it is tempting to speculate that this surface has a uniform termination. However, image simulations will be required to quantify the differences between these two structures with certainty.

#### (d) $\eta$ - $Mo_4O_{11}(100)$

The  $\eta$ - $Mo_4O_{11}(001)$  surface was imaged in air by STM. Like the other molybdate phases, cleavage revealed very flat surfaces and high resolution STM images could be formed by tunneling from filled states in the bias range of  $-0.29$  to  $-0.6$  V. Two typical images are shown in Fig. 9. All of the images of this surface, recorded with a variety of tips, have small regions that exhibit a regular, rectangular

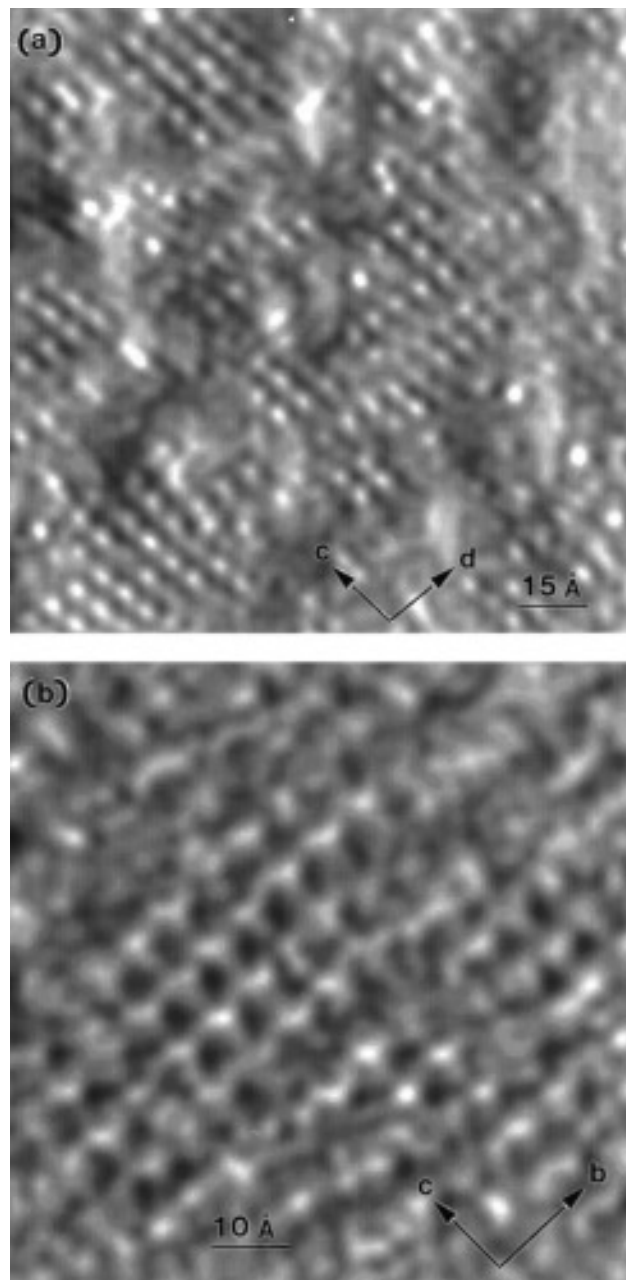


FIG. 9. STM images of the  $\eta$ - $Mo_4O_{11}(100)$  surface. (a) A  $140 \text{ \AA} \times 140 \text{ \AA}$  image recorded in UHV using a bias of  $-0.39$  V. The vertical height from black-to-white is  $1.5 \text{ \AA}$  (b) A  $80 \text{ \AA} \times 80 \text{ \AA}$  image recorded in air at a bias of  $-0.7$  V. The vertical height from black-to-white is  $1.5 \text{ \AA}$ .

array of white contrast features which are separated by regions of diffuse contrast and no recognizable order. Contact AFM imaging degraded this surface.

Although this is a three dimensionally bonded structure, we might expect that, in the ideal case, a uniform termination layer can be exposed. As mentioned in the introduction, we expect the cleaved (100) surfaces to be terminated at the planes which contain the  $MoO_4$  tetrahedra. The

bonds that must be broken to form this surface are axial linkages between a Mo atom at the center of an octahedron, an O at its apex, and a Mo atom at the center of a tetrahedron. The octahedral Mo–O bond is 2.11 Å and the tetrahedral Mo–O bond is 1.76 Å. Assuming that the longer and weaker of the two bonds is broken, the surface would be formed by a rectangular  $5.4 \times 6.7$  Å pattern of tetrahedral groups that are terminated by an apical O. The pattern of contrast observed in the ordered regions of the images has the same periodicity and there is a one-to-one correlation between the white spots and the expected positions of tetrahedral groups. Thus, the contrast in these images can be interpreted in the same way as the contrast in the images of all the other molybdates. We assume that the diffuse contrast arises from defects in this termination layer, which might react with the surrounding environment.

## DISCUSSION

The results presented above demonstrate that it is possible to use SPM to distinguish different types of surface/*CS* plane intersections in reduced Mo-oxides. The fully oxidized MoO<sub>3</sub>(010) surface is characterized by atomically flat terraces separated by steps that are integer multiples of 6.9 Å. When *CS* planes intersect the surface in such a way that a component of shear is normal to the surface plane, as it is for Mo<sub>18</sub>O<sub>52</sub>(100), 1.5 Å shear steps are clearly observed in SPM images. These features are easily discriminated from the much larger steps between the adjacent layers of the structure. When *CS* planes intersect the surface in such a way that the shear lies entirely in the surface plane, as it does in Mo<sub>8</sub>O<sub>23</sub>(010), the line of intersection is a dark contrast feature in STM images. Because we used compounds in which the orientation and distribution of the shear planes is known from bulk crystallography, we can take the assignments to be unambiguous. Furthermore, based on these assignments, it should also be possible to identify surface/*CS* plane intersections on inhomogeneously reduced materials where the features might have a much larger and irregular spacing.

It is interesting to note that while the surface/*CS* plane intersections appear as dark lines of contrast in all STM images of Mo<sub>8</sub>O<sub>23</sub>(010), there is no obvious topographic signature in the ideal structure. There are, however, structural elements that do not appear elsewhere. Within each cell, two groups of four edge-sharing octahedra are separated from one another by rectangular channels bounded by six octahedra. While most of the details of the contrast in Fig. 8a can be correlated with the expected positions of the different types of surface polyhedra, both types of polyhedra are expected at the surface/*CS* plane intersection and, therefore, the uniform dark appearance cannot be rationalized in the same way. If we instead assume that the contrast associated with these positions is due to an

electronic rather than a topographic effect, we would conclude that the local conductance is lower at the positions where the shear planes intersect the surface. This is consistent with the observation that the highest bulk electronic resistivity in this material is measured when the current travels parallel to the *CS* planes (32).

While the surface/*CS* plane intersections in all images of Mo<sub>18</sub>O<sub>52</sub>(100) are distinguished by the 1.5 Å vertical rise, and this alone is sufficient for identification, it is interesting to note that the spatially resolved tunneling spectra indicate that there is also an electronic effect. Specifically, the local conductance to the empty states at the surface/*CS* plane intersection is higher, in contrast to what we observed on the Mo<sub>8</sub>O<sub>23</sub>(010) surface. Because bulk data for the anisotropy of the electronic conductivity are not available for Mo<sub>18</sub>O<sub>52</sub>, we are not able to compare our local observation to the bulk result. It is noteworthy, however, that resistivity data for some shear compounds do show enhanced conductivity when the current travels parallel to the *CS* planes (33).

The anisotropy of the bonding in the four molybdates described here leads to the creation of stable surfaces that can be imaged in air and vacuum. The success of interpreting the observations simply by correlating the expected positions of surface polyhedra with the image contrast is somewhat surprising and raises some interesting questions. First, what are the differences between STM images recorded in UHV and those recorded in air? Ideally, we would like to be able to specify the surface structure as a function of the surrounding environment. However, the differences that we see in air and vacuum might be a reflection of the experimental conditions and active imaging mechanism rather than the surface structure. For example, when tunneling in air, we assume that the adsorbed layer of water that must be on the surface acts as a dielectric in the tunnel gap and modifies (increases) the tunneling probability.

There are two clear differences between the vacuum and air observations. First, on the Mo<sub>18</sub>O<sub>52</sub>(100) surface, contrast features corresponding to the tetrahedral groups were reproducibly observed only in vacuum. Second, the type of contrast exhibited in Fig. 8c (STM images of the Mo<sub>8</sub>O<sub>23</sub>(010) surface) was observed only in air. Unfortunately, it is not possible to attribute these differences solely to structural changes caused by the environment. In all of the cases described here, the absolute value of the bias used to record high resolution images in air is less than what is used in vacuum and all of the in air images were formed by tunneling from filled states. These are potentially important considerations since images recorded at different biases sample different energy levels which can potentially cause contrast differences. We can, however, make the statement that all images presented here were recorded while probing conduction band states formed by

the overlap of Mo and O orbitals. Because the Fermi level is pinned near the bottom of the conduction band, and this band is separated from the filled valence band by a gap of several volts, we do not probe the filled states even when the sample is negatively biased. We either tunnel to empty states above the Fermi level or remove electrons from filled states in the same band. However, differences might still arise because the relative contribution of the O orbitals to the density of states in the conduction band changes as a function of bias.

## CONCLUSIONS

Our findings indicate that the systematic SPM imaging of similar phases with well characterized structural differences is an effective way to develop contrast assignments. In this case, we have identified the contrast signatures of two different types of surface/*CS* plane intersections. Imaging and tunneling spectroscopy experiments indicate that these structural features have local electronic properties that differ from the rest of the surface. In our ongoing work, we are using these precedents to identify features on inhomogeneously reduced molybdate surfaces. Finally, we have also found that the details of the atomic-scale contrast can be interpreted based on naive models which assume that the structure of the cleaved surface can be predicted by assuming the cleavage of the longest, weakest bonds normal to the surface.

## ACKNOWLEDGMENT

This work was supported by the National Science Foundation under YIA Grant DMR-9458005.

## REFERENCES

1. J. Haber, in "Solid State Chemistry in Catalysis" (R. Grasselli and J. Brazdil, Eds.), p. 1. Am. Chem. Soc., Washington, DC, 1985.
2. J. M. Tatibouët and J. E. Germain, *J. Catal.* **72**, 375 (1981).
3. J. C. Volta and J. M. Tatibouët, *J. Catal.* **93**, 467 (1985).
4. K. Brückman, R. Grabowski, J. Haber, A. Mazurkiewicz, J. Sloczynski, and T. Wiltowski, *J. Catal.* **104**, 71 (1987).
5. W. E. Farneth, E. M. McCarron III, A. W. Sleight, and R. H. Staley, *Langmuir* **3**, 217 (1987).
6. R. L. McCormick and G. L. Schrader, *J. Catal.* **113**, 529 (1988).
7. B. Mingot, N. Floquet, O. Bertrand, M. Treilleux, J. J. Heizmann, J. Massardier, and M. Abon, *J. Catal.* **118**, 424 (1989).
8. L. A. Bursill, *Acta Crystallogr. Sect. A* **28**, 187 (1972).
9. P. L. Gai-Boyes, *Catal. Rev. Sci. Eng.* **34**, 1 (1992).
10. L. Kihlborg, *Ark. Kemi* **21**, 471 (1963).
11. L. Kihlborg, *Ark. Kemi* **21**, 357 (1963).
12. L. Kihlborg, *Ark. Kemi* **21**, 443 (1963).
13. L. Kihlborg, *Ark. Kemi* **21**, 461 (1963).
14. L. Kihlborg, *Ark. Kemi* **21**, 365 (1963).
15. L. Kihlborg, *Acta Chem. Scand.* **13**, 954 (1959).
16. L. E. Firment and A. Ferretti, *Surf. Sci.* **129**, 155 (1983).
17. L. C. Dufour, O. Bertrand, N. Floquet, *Surf. Sci.* **147**, 396 (1984).
18. L. E. Firment, A. Ferretti, M. R. Cohen, and R. P. Merrill, *Langmuir* **1**, 166 (1985).
19. O. Bertrand, N. Floquet, D. Jacquot, *Surf. Sci.* **164**, 305 (1985).
20. N. Floquet and O. Bertrand, *Surf. Sci.* **198**, 449 (1988).
21. N. Floquet and O. Bertrand, *Solid State Ionics* **32/33**, 234 (1989).
22. Y. Kim and C. M. Lieber, *Science* **257**, 375 (1992).
23. J. Heil, J. Wesner, B. Lommel, W. Assmus, and W. Grill, *J. Appl. Phys.* **65**, 5220 (1989).
24. E. Garfunkel, G. Rudd, D. Novak, S. Wang, G. Ebert, M. Greenblatt, T. Gustafsson, and S. H. Garofalini, *Science* **246**, 99 (1989).
25. G. Rudd, D. Novak, D. Saulys, R. A. Bartynski, S. Garofalini, K. V. Ramanujachary, M. Greenblatt, and E. Garfunkel, *J. Vac. Sci. Technol. B* **9**, 909 (1991).
26. U. Walter, R. E. Thomson, B. Burk, M. F. Crommie, A. Zettl, and J. Clarke, *Phys. Rev. B* **45**, 11474 (1992).
27. G. S. Rohrer, W. Lu, M. L. Norton, M. A. Blake, C. L. Rohrer, *J. Solid State Chem.* **109**, 359 (1994).
28. R. L. Smith, W. Lu, and G. S. Rohrer, *Surf. Sci.* **322**, 293 (1995).
29. G. S. Rohrer, W. Lu, R. L. Smith, and A. Hutchinson, *Surf. Sci.* **292**, 261 (1993).
30. G. Fourcaudot, J. Mercier, and H. Guyot, *J. Crystal Growth* **66**, 679 (1984).
31. O. Bertrand, N. Floquet, and D. Jacquot, *J. Crystal Growth* **96**, 708 (1989).
32. M. Greenblatt, *Chem. Rev.* **88**, 31 (1988).
33. M. Sato, M. Onoda, and Y. Matsuda, *J. Phys. C. Solid State Phys.* **20**, 4763 (1987).
34. M. D. Antonik and R. J. Lad, *J. Vac. Sci. Tech. A* **10**, 669 (1992).
35. C. F. Quate, *Surf. Sci.* **299/300**, 980 (1994).
36. S. N. Magonov and M-H. Whangbo, *Adv. Mater.* **6**, 335 (1994).
37. B. Parkinson, *J. Am. Chem. Soc.* **112**, 7498 (1990).